www.lajss.org
Latin American Journal of Solids and Structures 1 (2003) 75–100

Transient Green's Functions and Distributed Load Solutions for Plane Strain, Transversely Isotropic and Viscoelastic Layers

E. Mesquita[a,*], M. Adolph[a], P. L. A. Barros[b] and E. Romanini[c]

[a]Dept. of Computational Mechanics
State University at Campinas – Campinas – CP 6122 – SP – 13083-970 – Brazil
[b]Dept. of Geotechnics and Transportation
State University at Campinas – Brazil
[c]Dept. of Exact Sciences
CEUL – UFMS, Brazil

Abstract

The present article reports the numerical synthesis of transient Green's functions and distributed load solutions for transversely isotropic viscoelastic layers resting on a rigid bottom under plane strain conditions. Frequency domain solutions are used, in conjunction with the Fast Fourier Transform (FFT) algorithm, to render transient transversely isotropic viscoelastic responses. Accurate solutions at high frequency ranges allow the calculation of the transient response at very small time steps. A series of original results are reported. Transient displacement and traction Green's functions and transient displacement fields for distributed load solutions were determined. Short time and long term responses were obtained and explained in terms of the wave propagation and reflection phenomena. Snapshots of the displacement fields are furnished, allowing the visualization of the transient propagation phenomena. The obtained solutions make possible to assess the influence of viscoelastic models and parameters, as well as the degree of anisotropy of the continuum on the layer transient response. The constant hysteretic and the Kelvin-Voigt damping models are investigated. The effects of the viscoelastic models on the causality of the transient response are also addressed. The transient anisotropic viscoelastic solutions may be incorporated as auxiliary states in a Boundary Element solution strategy, allowing, for instance, the transient solution of rigid or flexible surface foundations interacting with a layer.

Keywords: Green's Functions, Transient Response, Viscoelasticity, Anisotropy, Layered media

1 Introduction

The dynamic response of unbounded domains, including soils, is accurately and efficiently described by the Boundary Element Method (BEM) [5, 6]. The two most striking advantages of

* Corresponding author Email: euclides@fem.unicamp.br Received 6 Oct 2003; In revised form 27 Oct 2003

applying the BEM to the unbounded domain dynamics are the reduction of the problem dimensionality and the natural fulfillment of the Sommerfeld Radiation Condition (SRC). Due to the first mentioned characteristic, only the boundary of the domains under consideration needs discretization, leading to faster meshing and smaller algebraic systems. The Sommerfeld radiation condition is the mathematical expression for the withdrawal of energy from the system by means of non-reflected waves propagating away from the source [21]. These two attributes render the BEM significant advantages compared to domain methods such as the Finite Element Method (FEM) [13].

The reduction of the problem dimension in the BEM formulation can only be accomplished if the Differential Equations (DE) governing the problem over a prescribed domain can be converted into a Boundary Integral Equation (BIE) without domain integrals. The transformation of the DE into the equivalent BIE is usually achieved with the aid of a vector identity or a reciprocal work theorem and requires an auxiliary state, which is usually a particular solution of the original DE [8]. Analogously, the BIE will only fulfill the Sommerfeld radiation condition if the employed auxiliary state also satisfies this condition [15]. The existence of the proper auxiliary state is a necessary condition to obtain the equivalent BIE without domain integrals. Distinct type of auxiliary states or solutions may be used to formulate the BIE. The solution of the DE for a point source in an unbounded domain, usually called a Fundamental Solution (FS), is presently the most common auxiliary state used to obtain the BIEs. The BEM may also be formulated using numerically synthesized auxiliary states, which can be the solution of concentrated or distributed loads [4].

The solution of viscoelastodynamic problems requires viscoelastodynamic auxiliary solutions. For stationary problems, described in the frequency or in the Laplace variable domain, the Fundamental Solutions or Green's functions may be readily obtained from the stationary elastic solutions by the elastic-viscoelastic correspondence principle [7]. For transient, time domain problems, a transient viscoelastic solution is required. Reference [10] synthesized a transient viscoelastic Fundamental Solution for the Maxwell model. They also developed some methodologies to evaluate the transient response of viscoelastic systems by the BEM. There are three main strategies, all based on the Laplace integral transform, to accomplish this task [9, 20]. For Boltzmann and Kelvin viscoelastic models, a promising time marching scheme has been proposed [16, 17]. But, up to the present time, there is no transient viscoelastic Fundamental Solution for the case of a general viscoelastic linear constitutive equation.

In the present article transient auxiliary states for viscoelastic and transversely isotropic layers under plane strain conditions and resting on a rigid base will be, exemplarily, synthesized. Displacement and traction kernels for concentrated load (Green's functions) and distributed load solutions are numerically determined.

These solutions are used to perform a series of parametric studies. The relation between the layer response and the wave propagation and reflection phenomena at the rigid bottom is analyzed. The effect of the layer anisotropy on the transient response is reported. The outlined procedure is applied to investigate the effects of two viscoelastic models and parameters on the

layer transient response. The constant hysteretic and the Kelvin-Voigt damping models are studied. The effects of the viscoelastic models on the causality of the transient response are also addressed.

2 Frequency Domain Solutions

The constitutive equations for two-dimensional transversely isotropic continua are given by [3]:

$$\left\{ \begin{array}{c} \sigma_{xx} \\ \sigma_{zz} \\ \sigma_{xz} \end{array} \right\} = \left[\begin{array}{ccc} c_{11} & c_{13} & 0 \\ c_{13} & c_{33} & 0 \\ 0 & 0 & c_{44} \end{array} \right] \left\{ \begin{array}{c} \epsilon_{xx} \\ \epsilon_{zz} \\ 2\epsilon_{xz} \end{array} \right\} \tag{1}$$

It is usual to describe the degree of anisotropy of the continuum by defining two indices, n_1 and n_3, which have unit values for the isotropic medium $n_1 = n_3 = 1$, and are defined in equations (2) for the transversely isotropic domain:

$$n_1 = c_{33}/c_{11}, \quad n_3 = (c_{11} - 2c_{44})/c_{13} \tag{2}$$

For the plain strain case and in the absence of body forces, the equations governing the continua in the frequency domain (ω) may be expressed in terms of the cartesian displacement components $\{u\} = \{u_x, u_z\}^t$ as:

$$\begin{aligned} c_{11}u_{x,xx} + c_{44}u_{x,zz} + (c_{13} + c_{44})u_{x,xz} + \rho\omega^2 u_x = 0, \\ c_{44}u_{z,xx} + c_{33}u_{z,zz} + (c_{13} + c_{44})u_{z,xz} + \rho\omega^2 u_z = 0 \end{aligned} \tag{3}$$

In equations (3) ρ is the continuum density and ω is the circular frequency.

Defining a set of dimensionless parameters

$$\alpha = \frac{c_{33}}{c_{44}}, \ \beta = \frac{c_{11}}{c_{44}}, \ \kappa = \frac{c_{13} + c_{44}}{c_{44}}, \ \delta^2 = \frac{\rho\omega^2}{c_{44}}, \tag{4}$$

equations (3) may be normalized to yield

$$\begin{aligned} \beta u_{x,xx} + u_{x,zz} + \kappa u_{z,xz} + \delta^2 u_x = 0, \\ u_{z,xx} + \alpha u_{z,zz} + \kappa u_{x,xz} + \delta^2 u_z = 0. \end{aligned} \tag{5}$$

The Fourier integral transform with respect to the pair (x, λ) may be applied on equations (5) leading to:

$$\begin{aligned} -\beta\lambda^2 \bar{u}_x + \bar{u}_{x,zz} + \mathrm{i}\kappa\lambda\bar{u}_{z,z} + \delta^2\bar{u}_x = 0, \\ -\lambda^2\bar{u}_z + \alpha\bar{u}_{z,zz} + i\kappa\lambda\bar{u}_{x,z} + \delta^2\bar{u}_z = 0, \end{aligned} \tag{6}$$

This set of coupled ordinary differential equations may be uncoupled leading to two linearly dependent ordinary equations in the displacement variable u_x and u_z:

$$\begin{aligned}\beta\lambda^4\bar{u}_x + \alpha\frac{\partial^4\bar{u}_x}{\partial z^4} - \gamma\lambda^2\frac{\partial^2\bar{u}_x}{\partial z^2} - (1+\beta)\lambda^2\delta^2\bar{u}_x + (1+\alpha)\delta^2\frac{\partial\bar{u}_x}{\partial z^2} + \delta^4\bar{u}_x = 0\\ \beta\lambda^4\bar{u}_z + \alpha\frac{\partial^4\bar{u}_z}{\partial z^4} - \gamma\lambda^2\frac{\partial^2\bar{u}_z}{\partial z^2} - (1+\beta)\lambda^2\delta^2\bar{u}_z + (1+\alpha)\delta^2\frac{\partial\bar{u}_z}{\partial z^2} + \delta^4\bar{u}_z = 0.\end{aligned} \tag{7}$$

The differential equations (7) possess a general solution in the form:

$$\begin{aligned}\bar{u}_z(\lambda,z) &= A_1\mathrm{e}^{-\delta\xi_1 z} + B_1\mathrm{e}^{\delta\xi_1 z} + A_2\mathrm{e}^{-\delta\xi_2 z} + B_2\mathrm{e}^{\delta\xi_2 z}.\\ \bar{u}_x(\lambda,z) &= A_1'\mathrm{e}^{-\delta\xi_1 z} + B_1'\mathrm{e}^{\delta\xi_1 z} + A_2'\mathrm{e}^{-\delta\xi_2 z} + B_2'\mathrm{e}^{\delta\xi_2 z}.\end{aligned} \tag{8}$$

Once the displacement solutions are known, the stress solutions may be obtained by using the Cauchy deformation tensor $\epsilon_{ij} = \frac{1}{2}\left(u_{i,j} + u_{j,i}\right)$ and applying the constitutive equation into the displacement equations (8). The stress solutions are:

$$\begin{aligned}\bar{\sigma}_{xx}\left(x,z,\omega\right) &= \sum_{m=1}^{2}(\eta_1 A_m\mathrm{e}^{-\delta\xi_m z} + \eta_2 B_m\mathrm{e}^{\delta\xi_m z}),\\ \bar{\sigma}_{xz}\left(x,z,\omega\right) &= \sum_{m=1}^{2}(\eta_3 A_m\mathrm{e}^{-\delta\xi_m z} + \eta_4 B_m\mathrm{e}^{\delta\xi_m z}),\\ \bar{\sigma}_{zz}\left(x,z,\omega\right) &= \sum_{m=1}^{2}(\eta_5 A_m\mathrm{e}^{-\delta\xi_m z} + \eta_6 B_m\mathrm{e}^{\delta\xi_m z})\end{aligned} \tag{9}$$

The factors ξ_1 and ξ_2 in equation (8) and (9) are the eigenvalues of the coupled operator shown in equations (6). Detailed expressions for the functions $\eta_i(\lambda)$, $(i = 1, 6)$ present in (9) and (11) may be found in [2, 3]. Through a numerical inverse Fourier transformation of equations with respect to the pair (λ, x), the displacement solution in the original space-frequency domain (x, z, ω) may be determined:

$$\begin{aligned}u_x\left(x,z,\omega\right) &= \frac{\delta}{\sqrt{2\pi}}\int_{-\infty}^{\infty}\sum_{m=1}^{2}\left(A_m'\mathrm{e}^{-\delta\xi_m z} + B_m'\mathrm{e}^{\delta\xi_m z}\right)\mathrm{e}^{\mathrm{i}\lambda x}\mathrm{d}\lambda\\ u_z\left(x,z,\omega\right) &= \frac{\delta}{\sqrt{2\pi}}\int_{-\infty}^{\infty}\sum_{m=1}^{2}\left(A_m\mathrm{e}^{-\delta\xi_m z} + B_m\mathrm{e}^{\delta\xi_m z}\right)\mathrm{e}^{\mathrm{i}\lambda x}\mathrm{d}\lambda\end{aligned} \tag{10}$$

Analogously for the stresses:

$$\sigma_{xx}(x,z,\omega) = \frac{\delta}{\sqrt{2\pi}} \int_{-\infty}^{\infty} \sum_{m=1}^{2} \left(\eta_1 A_m \mathrm{e}^{-\delta\xi_m z} + \eta_2 B_m \mathrm{e}^{\delta\xi_m z} \right) \mathrm{e}^{\mathrm{i}\lambda x} \mathrm{d}\lambda$$

$$\sigma_{xz}(x,z,\omega) = \frac{\delta}{\sqrt{2\pi}} \int_{-\infty}^{\infty} \sum_{m=1}^{2} \left(\eta_3 A_m \mathrm{e}^{-\delta\xi_m z} + \eta_4 B_m \mathrm{e}^{\delta\xi_m z} \right) \mathrm{e}^{\mathrm{i}\lambda x} \mathrm{d}\lambda$$

$$\sigma_{zz}(x,z,\omega) = \frac{\delta}{\sqrt{2\pi}} \int_{-\infty}^{\infty} \sum_{m=1}^{2} \left(\eta_5 A_m \mathrm{e}^{-\delta\xi_m z} + \eta_6 B_m \mathrm{e}^{\delta\xi_m z} \right) \mathrm{e}^{\mathrm{i}\lambda x} \mathrm{d}\lambda \tag{11}$$

It should be clear that the constants A_m, A'_m, B_m and B'_m are to be determined from the boundary conditions imposed to the problem.

2.1 Viscoelastic Models

Viscoelastic behavior is introduced through the elastic-viscoelastic correspondence principle [7] by making the elastic constants complex:

$$c^*_{ij} = c^*_{1ij}(\omega) + \mathrm{i}c^*_{2ij}(\omega) = c^*_{1ij}(\omega)\left[1 + \mathrm{i}\eta_{ij}(\omega)\right], \quad ij = 11, 33, 13, 44 \tag{12}$$

In equation (12) the indicated quantities define a storage modulus $c^*_{1ij}(\omega)$, a loss modulus $c^*_{2ij}(\omega)$ and a damping factor $\eta_{ij}(\omega) = c^*_{2ij}(\omega)/c^*_{1ij}(\omega)$. In this article the storage moduli are considered constant and possessing the value of the elastic counterpart, $c^*_{111}(\omega) = c_{11}$, $c^*_{133}(\omega) = c_{33}$, $c^*_{113}(\omega) = c_{13}$, $c^*_{144}(\omega) = c_{44}$. The damping factors are considered equal $\eta_{11}(\omega) = \eta_{33}(\omega) = \eta_{13}(\omega) = \eta_{44}(\omega)$. Two distinct viscoelastic damping models are investigated, namely the constant hysteretic model, $\eta(\omega) = \eta = \mathrm{cte}$, and the Kelvin-Voigt model, $\eta(\omega) = \eta\omega$. Typical frequency content of the investigated damping factors is shown in Figure 1.

2.2 Boundary Conditions for the frequency domain Green's function

Initially a vertical concentrated point load is applied at the surface of the layer, as indicated in Figure 2(a). The mathematical expressions for the boundary conditions are:

$$\begin{aligned} &\sigma_{zz}(x, z=0) = -\delta(x) \\ &\sigma_{xz}(x, z=0) = 0 \\ &u_x(x, z=H) = u_z(x, z=H) = 0 \end{aligned} \tag{13}$$

Applying the four boundary conditions described by equations (13) into equations (8) and (9) will result in a 4×4 algebraic system for the constants A_m, A'_m, B_m and B'_m. Once this system is analytically or numerically solved, the resulting expressions may be inserted into equations (10) and (11), which, in turn, can be numerically evaluated. The procedure will produce frequency dependent displacement $u_{gz}(x,z,\omega)$, $u_{gx}(x,z,\omega)$ and traction $\sigma_{gzz}(x,z,\omega)$, $\sigma_{gxz}(x,z,\omega)$, $\sigma_{gxx}(x,z,\omega)$ Green's functions for the layer.

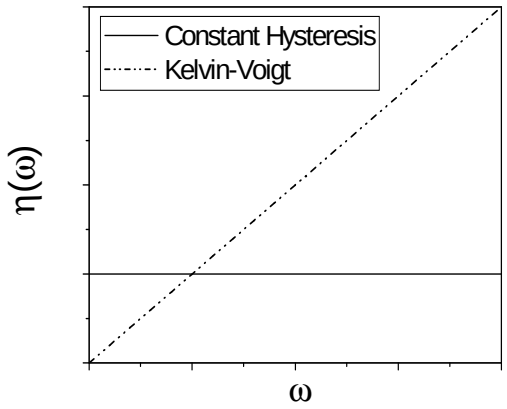

Figure 1: Typical frequency content of the damping factor $\eta(\omega)$ for distinct viscoelastic models

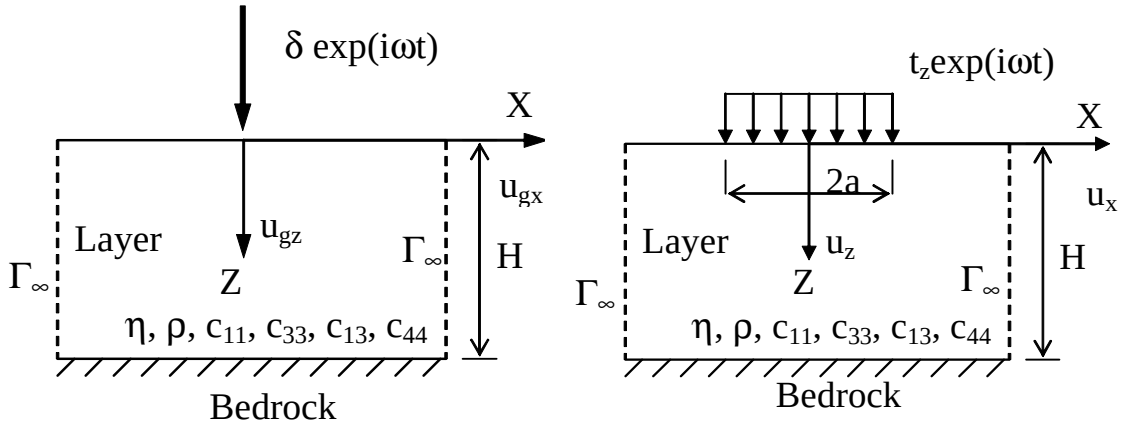

(a) Concentrated load or Green's function

(b) Distributed load

Figure 2: Boundary conditions for the Stress Boundary Value problems

2.3 Boundary Conditions for the frequency domain distributed load solutions

Figure 2(b) shows, schematically, the traction boundary conditions (BCs) for the distributed load solutions. It consists of a spatially constant vertical stress distribution σ_{zz} of width $2a$, applied at the layer surface. The mathematical expressions for these BCs are:

$$\begin{aligned}
&\sigma_{zz}\left(x, z=0\right) = \begin{cases} -t_z; & |x| \leq a \\ 0; & |x| > a \end{cases} \\
&\sigma_{xz}\left(x, z=0\right) = 0 \\
&u_x\left(x, z=H\right) = u_z\left(x, z=H\right) = 0
\end{aligned} \tag{14}$$

These boundary conditions may also be applied to equations into (8) and (9) resulting into an algebraic system for the constants A_m, A'_m, B_m and B'_m. Detailed expressions for the constants may be found in [2, 3].

2.4 Numerical results in the frequency domain

A numerical integration strategy has been developed to solve equations (10) and (11) yielding accurate solutions at very high frequencies. The frequency solutions were already validated in previous works [2, 3]. Figure 3 shows a typical vertical displacement solution $u_z(A_0)$ resulting from the distributed load condition and plotted for the dimensionless frequency $A_0 = \omega a\sqrt{\rho/c_{44}}$. The layer resonances in the vertical direction are clearly recognized in the solution. It should be stressed that from the physical point of view almost all significant phenomena take place at relative low frequencies $A_0 < 10$ [11]. The high frequency components are calculated to provide small time-steps for the transient response. The frequency solutions given in Figures 3 were determined for an isotropic continua ($n_1 = n_3 = 1$), for a layer depth $H = 4a$ and for a constant hysteretic viscoelastic model with damping factor $\eta = 0.05$. Figures 3 also show that the dynamics of a layer over bedrock is quite involved. This intrincated behavior is also present in the transient response.

3 Synthesis of Transient Responses

The transient solution is obtained by applying the Fast Fourier Transform (FFT) algorithm with respect to the pair (ω, t) to the solutions furnished by equations (10) and (11). One important issue of the discrete FT is the relation between the frequency step $\Delta\omega = \omega_{k+1} - \omega_k$ and the maximum time reachable in the transient process, $T_{\max} = 2\pi/\Delta\omega$. Analogously, the relation between the time step Δt and the maximum sampling frequency $\omega_{\max}$ is: $\Delta t = 2\pi/\omega_{\max}$. It is desirable to have frequency solutions at very small steps $\Delta\omega$ leading to very long $T_{\max}$ and also solutions determined at very large maximum sampling frequencies $\omega_{\max}$, resulting in small time steps Δt. However, it should be stressed that the determination of frequency domain solutions is computationally very expensive. In order to yield small steps and large final frequencies, the

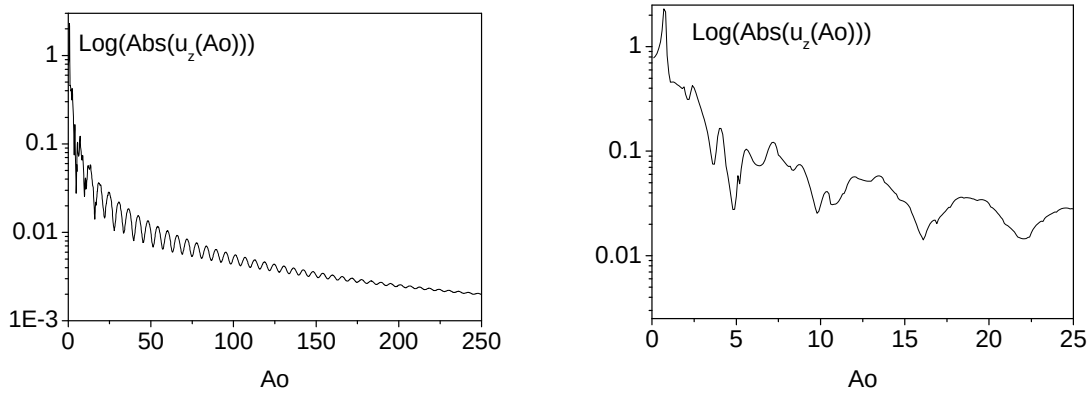

(a) Large frequency solution

(b) Detail of the initial frequency steps

Figure 3: Stationary vertical displacement solution u_z due to a distributed surface load t_z

frequency domain solutions $u_i(\omega)$ must undergo a mathematical treatment. Starting from this point, the reasoning based on the circular frequency ω will be applied to dimensionless frequency parameter $A_0 = \omega a \sqrt{\frac{\rho}{c_{44}}}$.

Figure 4 shows, schematically, the mathematical manipulation that is applied to the frequency solutions. The functions $u_i(A_0)$ $(i = x, z)$ are calculated numerically, with a frequency step ΔA_0 in the range $0 < A_0 < A_{0-\text{calc}}$. To obtain a smaller frequency step in this range, the function is interpolated with cubic splines. Beyond the frequency $A_{0-\text{calc}}$, the numerical integration scheme fails or it is extremely time consuming. Above the cut-off frequency $A_{0-\text{zero}}$ the functions are assumed to vanish, $u_i(A_0 > A_{0-\text{zero}}) = 0$. In the range between $A_{0-\text{calc}} < A_0 < A_{0-\text{zero}}$ the functions are also interpolated by cubic splines, leading to a smooth transition between the frequency points $A_{0-\text{calc}}$ and $A_{0-\text{zero}}$. For low damping values, the stationary response presents high oscillations at $A_{0-\text{calc}}$. In this case splines do not lead to a smooth transition and an exponential filter can be applied to enforce transition smoothness [1].

Above the cut-off frequency $A_{0-\text{zero}}$, the solution is filled with zeros $u_i(A_{0-\text{zero}} < A_0 < A_{0f}) = 0$. If all significant information from the frequency signals has been determined in the range $0 < A_0 < A_{0-\text{zero}}$, then filling the response with zeros should only lead to smaller time steps, without changing the transient response itself. This effect is shown in Figure 5 for a typical vertical transient solution $u_z(\tau) = u_z \frac{c_{44}}{a t_z}$ for the dimensionless time instants $\tau = \frac{t}{a}\sqrt{\frac{c_{44}}{\rho}}$, at which the response reaches a peak. For this case, the distributed load solution was considered. The constant hysteretic model with damping $\eta = 0.05$ was used and the considered layer depth is $H = 4a$. The layer is considered isotropic $n_1 = n_3 = 1$. For this example the solution is numerically calculated up to the frequency $A_{0-\text{calc}} = A_{0-\text{zero}} = 1000$. No smoothing transition procedure has been applied between $A_{0-\text{calc}}$ and $A_{0-\text{zero}}$. Beyond $A_{0-\text{zero}}$ the solution is filled

with zeros up to the frequency A_{0-f}. Four distinct values of the maximum frequency were considered in the analysis: $A_{0-f1} = 1638.4$, $A_{0-f2} = 3276.8$, $A_{0-f3} = 6553.6$, $A_{0-f4} = 13107.2$. The frequency step is $\Delta A_0 = 0.0125$, leading to four distinct final number of discrete sampling points k given, respectively, by: $k_1 = 131072$, $k_2 = 262144$, $k_3 = 262144$, $k_4 = 1048576$. An analysis of Figure 5 shows, as expected, that adding zeros to the end of the response spectrum only leads to smaller time steps, without changing the transient response itself.

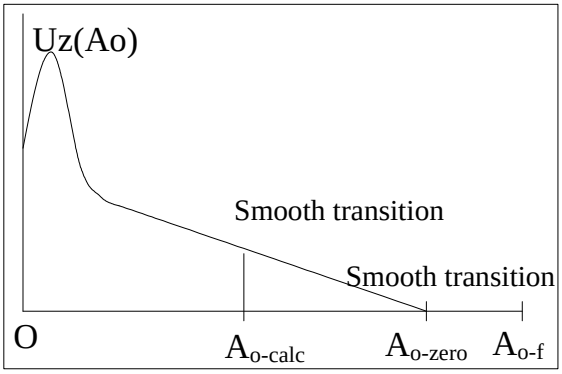

Figure 4: Scheme for treating the frequency solutions

Next, the influence of the frequency step ΔA_0 is addressed. The frequency response was calculated with three steps, namely $\Delta A_0 = 0.05$, $\Delta A_0 = 0.025$ and $\Delta A_0 = 0.0125$. To obtain the smaller frequency steps the results from the original calculation ($\Delta A_0 = 0.05$) were interpolated with cubic splines. If the original frequency step is able to retain all significant signal information, the interpolation itself should only lead to larger final times $T_{\max}$ but should not alter the response at the initial instants. Figure 6 shows this effect on the transient response. It can be seen that as ΔA_0 decreases the maximum time $T_{\max}$ increases proportionally, as expected. No significant signal distortion is introduced by decreasing the frequency step, as can be seen in Figure 6, for the initial response instants.

Figure 6 also allows to consider the quality of the transient response numerically obtained. It has very small time steps and extremely large final times. No other numerical procedure is, presently, able to furnish this quality of results for unbounded domains.

4 Numerical Results

Initially the results for the numerically synthesized transient responses will be validated. Considering that there are no transient solutions available for viscoelastic and anisotropic layers, the validation will performed only for the isotropic case, $n_1 = n_3 = 1$, and also only for the initial instants, that is, before the first wave reaches the bottom of the layer and is reflected back to

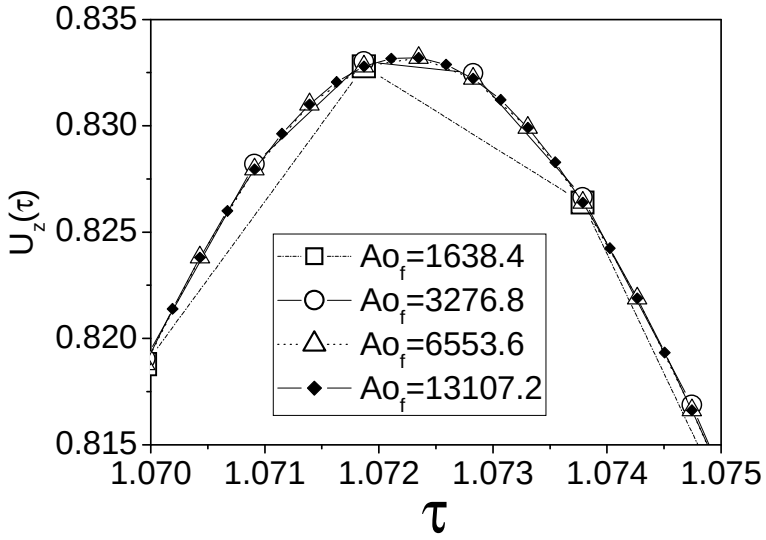

Figure 5: Effect of including zeros between $A_{0-\text{zero}} < A_0 < A_{0f}$.

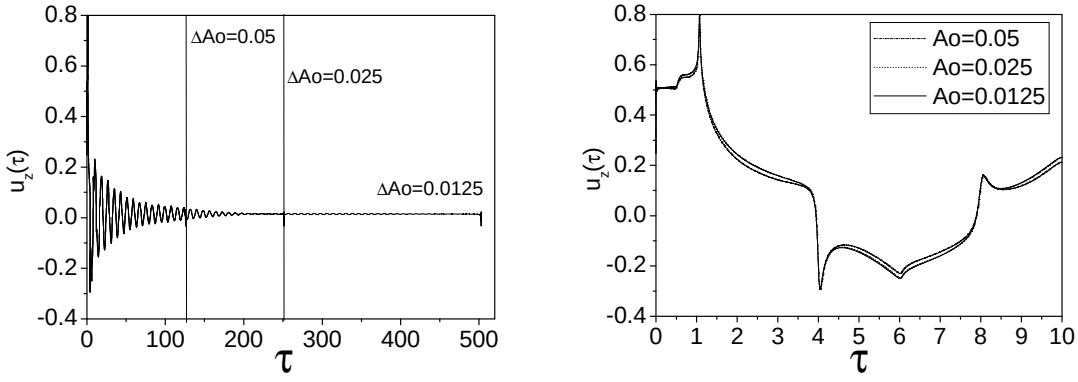

(a) Overview of time response

(b) Initial time instants

Figure 6: Influence of the frequency step ΔA_0 on the transient response

the surface. Under these conditions the obtained layer solution should equal the solution for the elastic half-space [18, 19]. For larger periods of time the solution will be correlated to the wave propagation process taking place at the excited layer.

4.1 Validation. Short time response for the Green's function.

Two short time responses are compared with data available in the literature. Figures 7(a) and 7(b) show the excitation and measuring points for the validation examples. In the first case a point at the origin ($x = z = 0$) is excited by a Dirac's pulse, $f(t) = \delta(t)$. The transient response is measured at point 1 with coordinates ($x = 0, z = a$). The response of the dimensionless vertical component $u_{gz}(x = 0, z = a, \tau)$ is given in Figure 8, for three distinct layer depths ($H = 2a, 4a, 8a$). The layer parameters are: $c_{11}/c_{44} = 3, n_1 = n_3 = 1$. The constant hysteretic viscoelastic model with damping factor $\eta = 0.2$ was applied. To obtain the transient solution the following frequency parameters were adopted: $A_{0-\text{calc}} = A_{0-\text{zero}} = 150$ and $A_{0-f} = 409.575$, $\tau_{\max} = 251.32$, $\Delta\tau = 0.0077$.

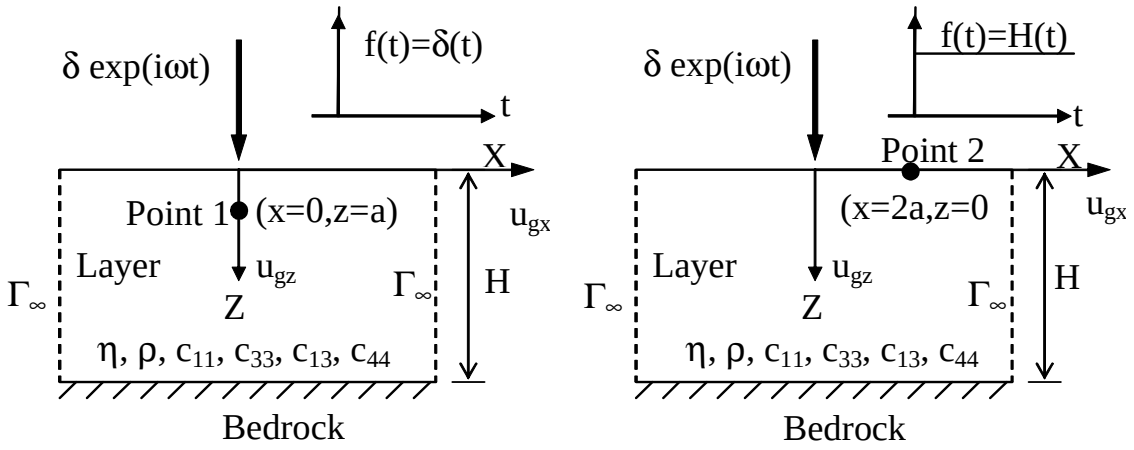

(a) Point 1 - Dirac excitation

(b) Point 2 - Heaviside excitation

Figure 7: Excitations and measuring points for the validation of short time responses

An analysis of Figure 8 reveals that, at the initial instants, the reported numerical results agree very well with the elastic half-space solution [18, 19]. The vertical displacement due to reflections at the bottom and at the layer free surface is clearly recognized. As the layer grows deeper, the wave reflection occurs at later times and the displacement amplitude is attenuated by the viscoelastic effects of the medium , as expected.

For the second validation case, shown in Figures 7(b) and 9, the point at the origin is excited by a unit step function (Heaviside function), $f(t) = H(t)$. The solution is measured at the point 2, with coordinates ($x = 2a, z = 0$). The vertical transient response $u_{gz}(x = 2a, z = 0, \tau)$ is shown in Figure 9. The half-space isotropic elastic solution obtained by Guan and Novak [12] and

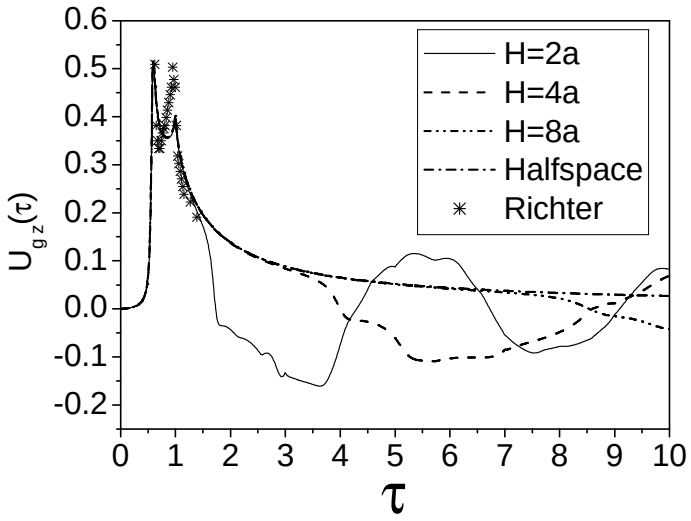

Figure 8: Validation of the transient Green's function vertical component $u_{gz}\,(x=0, z=a, \tau)$

by Mesquita et alii [17] are also reported. The continuum properties are: $c_{11}/c_{44}=4, n_1=n_3=1$. The numerical solutions were obtained for the same frequency parameters of the previous case. An analysis shows clearly that viscoelastic solutions present lower peak amplitudes. The reflection due to the layer bottom and free surface are also well depicted in the transient response.

The examples above indicate that the responses at initial time instants are consistent. Aiming to furnish an overview of the wave propagation phenomena due to the excitation given in Figure 7(a), a series of four snapshots for the vertical displacement field $u_{gz}(x,z,\tau)$ of an isotropic viscoelastic layer is given in Figures 10. The propagation of the faster compressional wave (p) can be easily recognized. The Rayleigh surface waves are also well characterized.

4.2 Analysis. Short time response for the distributed load solution

The transient response of a point located at the center of the loading area ($x=z=0$) will be correlated to the wave propagation process taking place at the excited layer. Consider an isotropic viscoelastic layer ($n1=n3=1$) with depth $H=4a$, possessing hysteretic damping $\eta=0.05$ and elastic constitutive parameters $c_{11}/c_{44}=4$, subjected to the uniformly distributed spatial load, given in equation (14), and a Dirac's Delta impulse in time $f(t)=\delta(t)$. With these constitutive parameters the layer presents a dimensionless dilatational wave velocity $p_1=2$, shear velocity $c_1=1$ and a Rayleigh wave velocity $c_R\approx 0.95$. In the range $(0<A_0<A_{0-\mathrm{calc}})$ the stationary responses were generated with a dimensionless frequency step $\Delta A_0=0.0125$. The

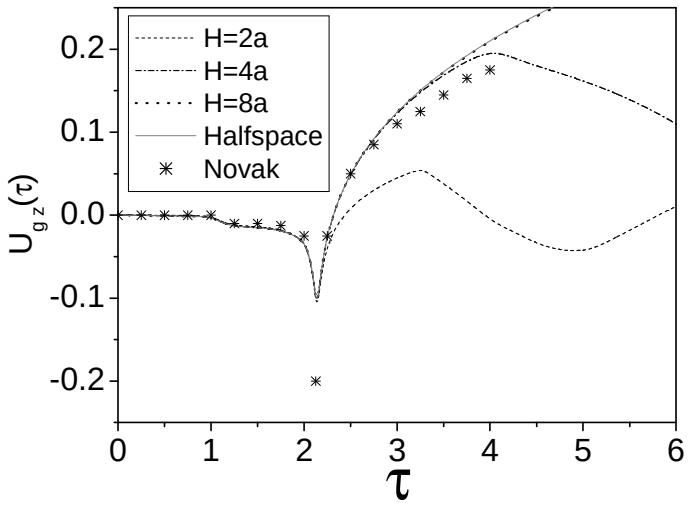

Figure 9: Validation of the transient Green's function vertical component $u_{gz}\,(x = 2a, z = 0, \tau)$

other frequency parameters are $A_{0-\text{calc}} = A_{0-\text{zero}} = 1000$, $A_{0-f} = 1638.4$. A total of 131072 frequency terms were used. The correspondent transient response has a period $\tau_{\max} = 502.65$ and a time step $\Delta\tau = 0.019$.

Figure 11 furnishes the transient vertical displacement $u_z(x = z = 0, \tau)$ for the initial time instants. A sequence of snapshots showing the evolution of the layer vertical displacement component $u_z(x, z, \tau)$ at these initial instants, depicted in Figures 12, explains the response obtained in Figure 11. After a very abrupt initial response ($\tau = 0 + \Delta\tau$) the displacement remains almost stable at the value $u_z \approx 0.5$, until approximately $\tau \approx 0.5$ when there is a slight increase in the displacement, due to p-waves arriving from the corners of the spatial excitation. The displacement continues stable at this level until the sequence or train of shear-waves (c) and Rayleigh-waves also generated at the corners of the spatial excitation arrive, inducing an amplitude peak at approximately $\tau \approx 1.1$. After this peak the displacement amplitude decreases monotonically until the first reflected wave arrives, as will be described in the sequence.

4.3 Analysis. Long term response for the distributed load solution

To analyze the transient behavior at larger time periods, the wave reflections at the rigid base must be considered. Figure 13 shows the transient response at the origin ($x = z = 0$) of a layer over bedrock with depth $H = 2a$. This figure also shows the transient response of a half-space, in which no waves are reflected back to the surface. To interpret these results, a

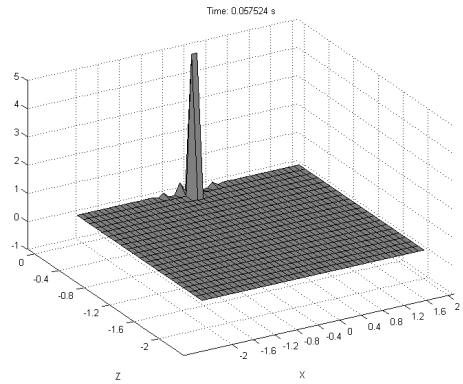

(a) $\tau = 0.057524$

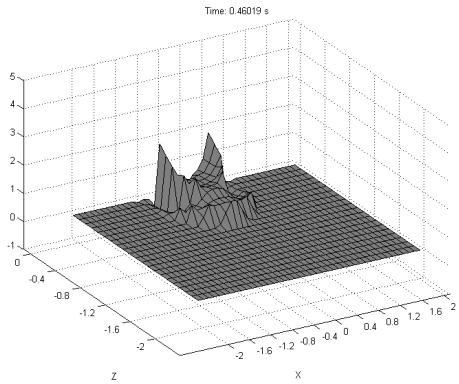

(b) $\tau = 0.46019$

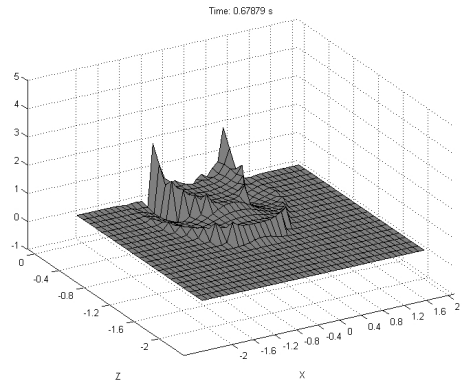

(c) $\tau = 0.67379$

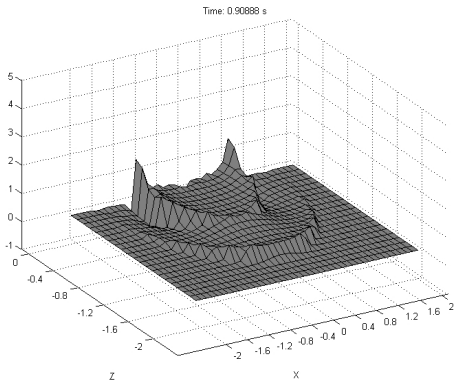

(d) $\tau = 0.90388$

Figure 10: Transient vertical displacement field $u_{gz}(x, z, \tau)$ of the layer

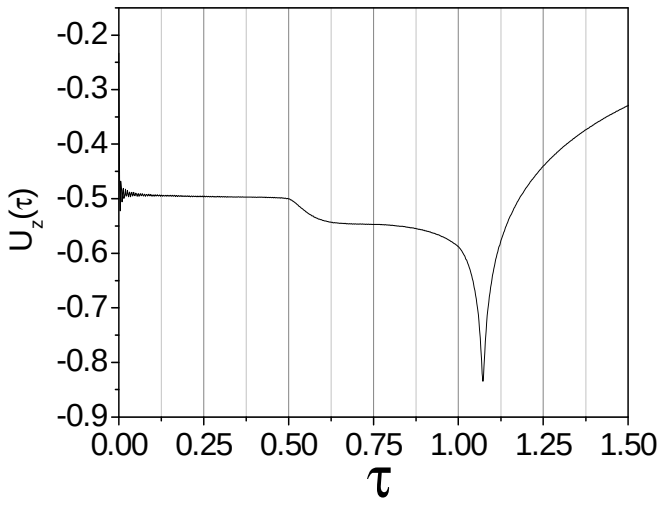

Figure 11: Initial time steps of the layer transient response

scheme containing some possible trajectories of waves emanating from the surface and reflected at the rigid base is given in Figure 14. The idea is to indicate that as the spatial excitation distribution is continuous, the reflected waves will also arrive continuously at the measuring point ($x = z = 0$), breaking the original sharp wave fronts of the Green's solutions.

Figures 15 show, schematically, the pattern of wave propagation and reflection at various time instants for a layer with depth $H = 2a$. It is known that at the initial time instants p-waves (dilatational) and c-waves (shear) are sent towards the rigid base with velocities $p_1 = 2$ and $c_1 = 1$, respectively. Surface Rayleigh waves are kept close to the surface and will not be included in propagation pattern. At time $\tau = 1$ the p_1 wave reaches the rigid base ($H = 2a$) and is reflected back as a dilatational p_{p1} wave and as a shear wave c_{p1}. At time $\tau = 2$ the p_{p1} wave reaches back the layer surface. At this same instant the c_1 wave also reaches the bottom and is reflected as a dilatational p_{c1} and a c_{c1} shear wave. The influence of p_{p1} reaching back the surface as a traction wave can readily be recognized in Figure 13. The propagation pattern may be followed correlating Figures 13 and 15. The arrival of c_{p1} and p_{c1} at $\tau = 3$ is clear at the picture. At $\tau = 4$ the p_{ppp1} and c_{c1} reaches the surface, and so on. In the context of the present article it is important to recognize that all these features are present in the numerically determined transient solution, exemplarily, given in Figure 13.

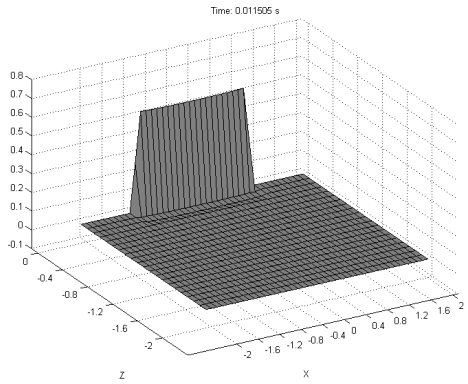

(a) $\tau = 0 + \Delta\tau$

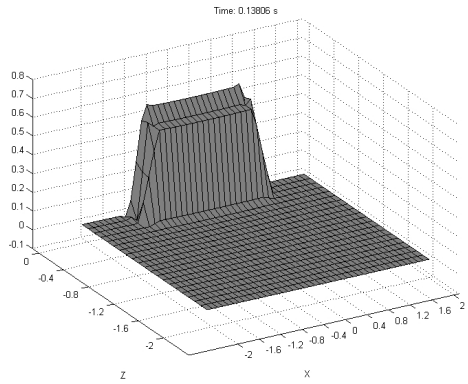

(b) $\tau = 0.13806$

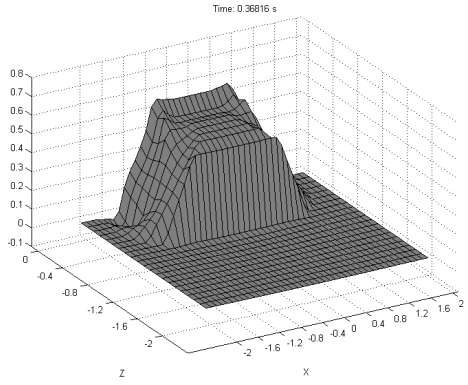

(c) $\tau = 0.36816$

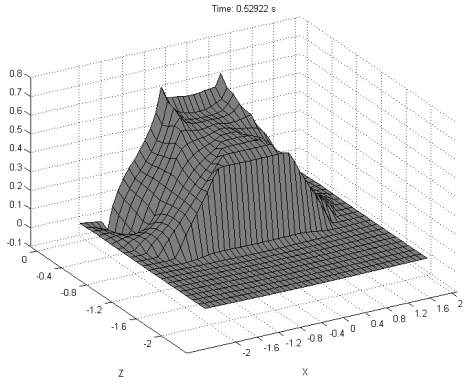

(d) $\tau = 0.52155$

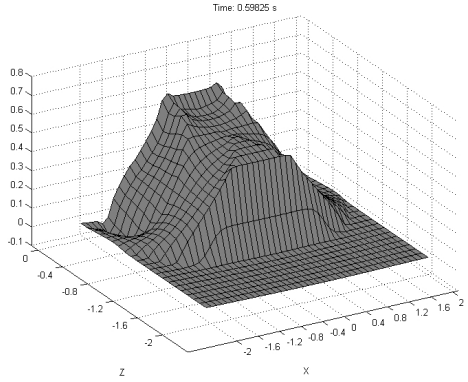

(e) $\tau = 0.59825$

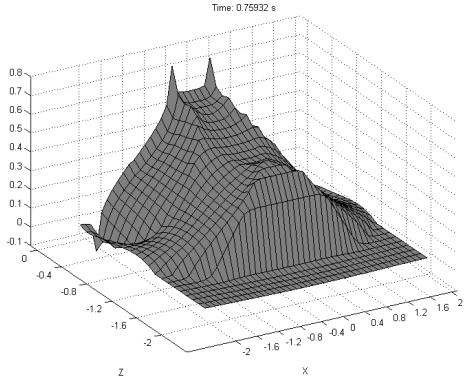

(f) $\tau = 0.75165$

Figure 12: Transient vertical displacement field $u_z(x, z, \tau)$

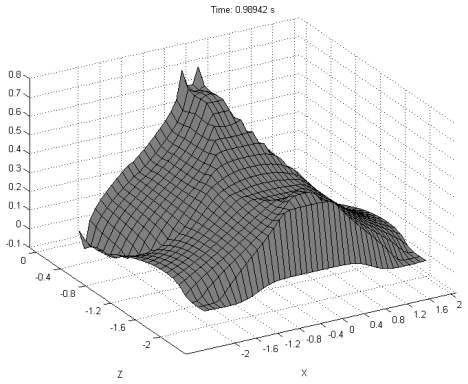

(g) $\tau = 0.98175$

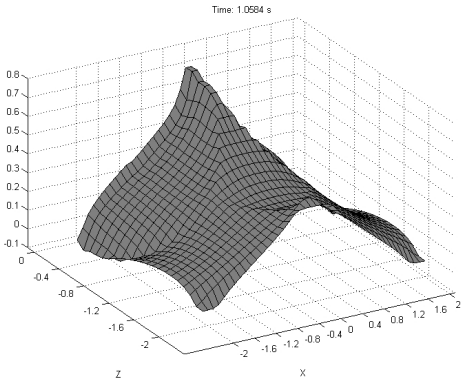

(h) $\tau = 1.0584$

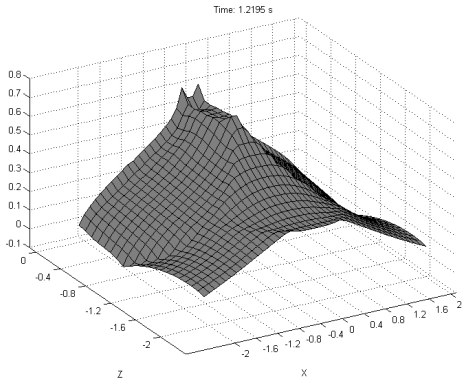

(i) $\tau = 1.2118$

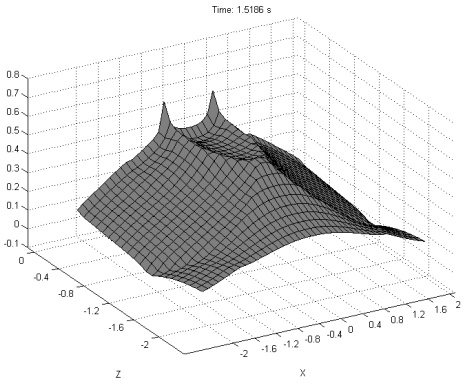

(j) $\tau = 1.5186$

Figure 12: Transient vertical displacement field $u_z(x, z, \tau)$ (continued)

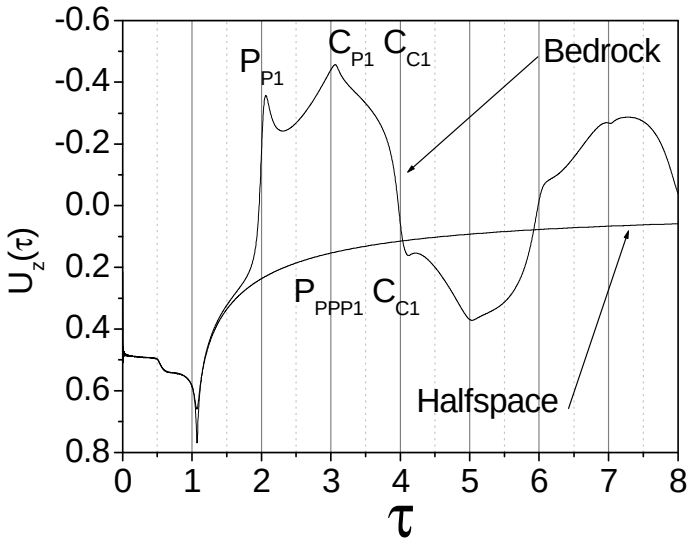

Figure 13: Long term response of a layer over bedrock, $H = 2a$

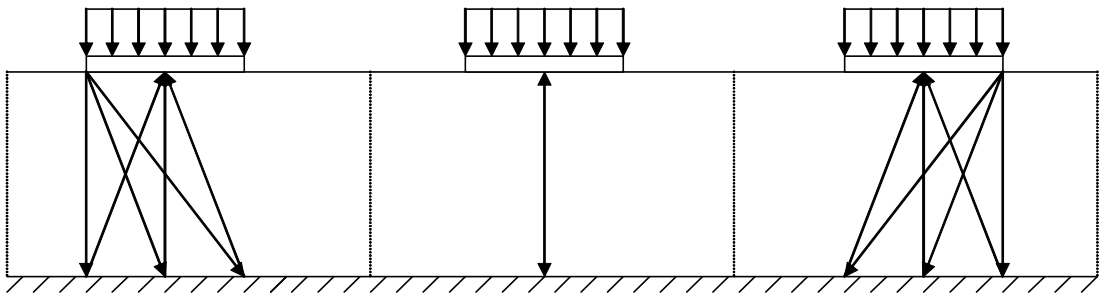

Figure 14: Trajectories of waves reflected at the layer rigid base

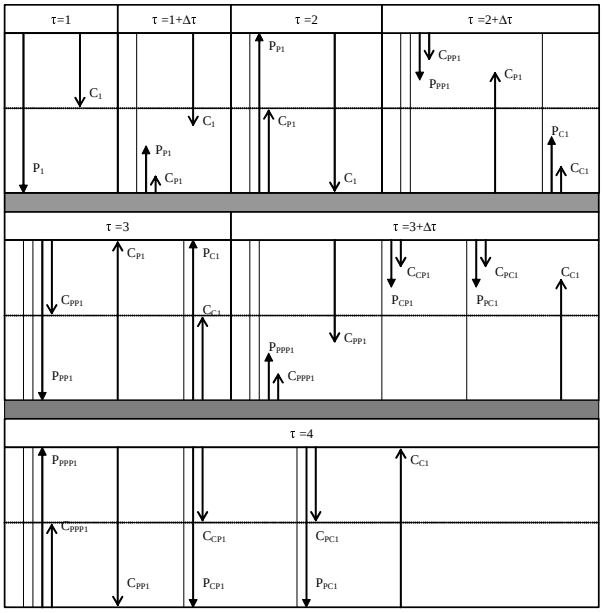

Figure 15: Scheme of wave propagation and reflection at the rigid base and surface for distinct time instants

4.4 Analysis. Traction solutions for the Green's function

Up to this point, only displacement solutions have been reported. In this section a transient stress solution is synthesized. The considered layer is isotropic $n_1 = n_3 = 1$ with $c_{11}/c_{44} = 3$. Hysteretic damping with $\eta = 0.2$ is adopted. The spatial and temporal excitations are Dirac's Delta (see Figure 7(a)). The frequency parameters are: $A_{0-\text{calc}} = A_{0-\text{zero}} = 1000$, $A_{0-f} = 3272.8$. Two distinct layer depths are examined, $H = 2a, 4a$. The response is measured at point 1, with coordinates $x = 0$, $z = a$.

Figure 16 shows the transient component of the normalized stress solution $\sigma_{gxx}(\tau)$ for the two layers under analysis. A numerically synthesized solution for the half-space case is also included. Analogously, Figure 17 shows the stress component $\sigma_{gzz}(\tau)$. The arrival of the dilatational and shear stress waves are vividly depicted. For the half-space solution only two wave fronts are noticeable. For the layer, the reflections at the rigid base and at the free surface induce other stress wave fronts, which are periodical and with decreasing amplitude due to the material and geometric damping present in the solution. The arrival time for the multiple wave fronts can be correlated to the dilatational and shear wave velocities. The high quality of the obtained results is corroborated by the large gradients of the stress fields present in the solution. For the best of the authors' knowledge, as in most of the previous cases, there are no results available in the literature that would allow a validation of the determined stress solutions.

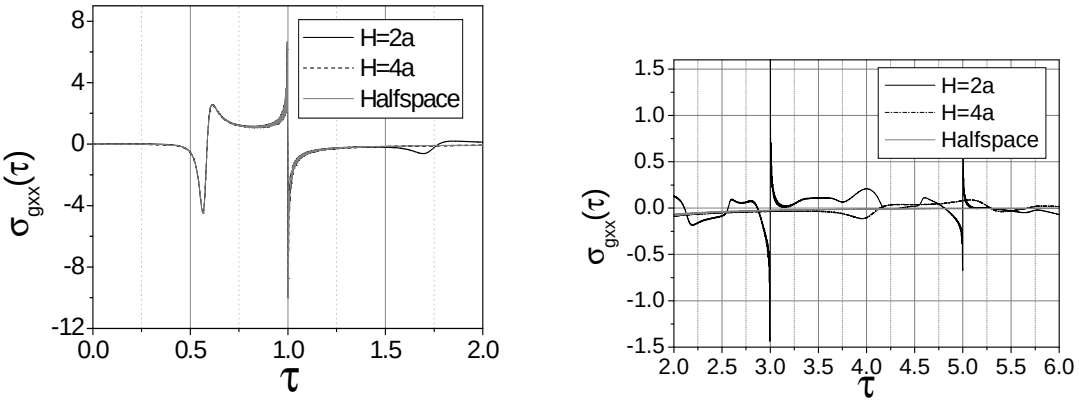

Figure 16: Transient stress component $\sigma_{gxx}(\tau)$ for the Green's function

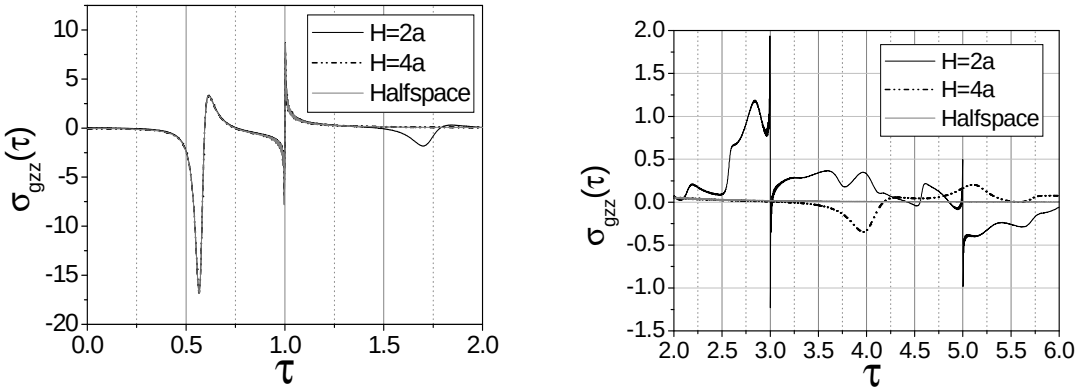

Figure 17: Transient stress component $\sigma_{gzz}(\tau)$ for the Green's function

4.5 Influence of the viscoelastic model on the transient response.

In the sequence, the effect of the viscoelastic models and damping parameters on the transient response is investigated. Consider an isotropic viscoelastic layer with $H = 4a$ and the same material properties of the example shown in Figure 13, subjected to a Dirac's Delta $f(t) = \delta(t)$. Two damping models, namely, the constant hysteretic and the Kelvin-Voigt, with damping coefficients $\eta = 0.05, 0.1, 0.2$ are investigated. Figure 18 shows the influence of the damping parameter for the constant hysteretic model. As expected, increasing the damping will lead to smaller displacement amplitudes. The same response for a Kelvin-Voigt model is depicted in Figure 19.

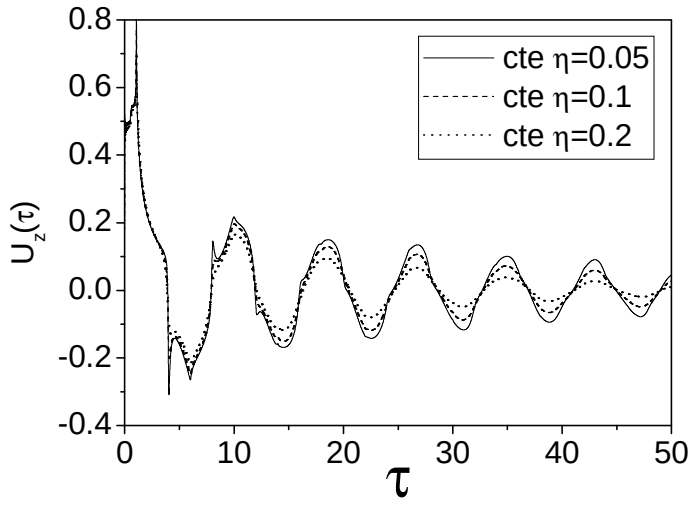

Figure 18: Displacement $u_z(\tau)$ as a function of the damping coefficient η-constant hysteretic model

4.6 Influence of the layer depth.

As can be seen in Figure 20, the layer depth causes two distinct effects on the transient response. For deeper layers the path that must be traveled by the waves prior to the arrival back at the surface increases. The consequences are that the reflected waves impinge the surface at later times with smaller amplitudes, due larger energy dissipation (geometric and internal). All these phenomena are well characterized in the response shown in Figure 20. The example considered a hysteretic damping with $\eta = 0.1$. Other properties are those of the previous examples.

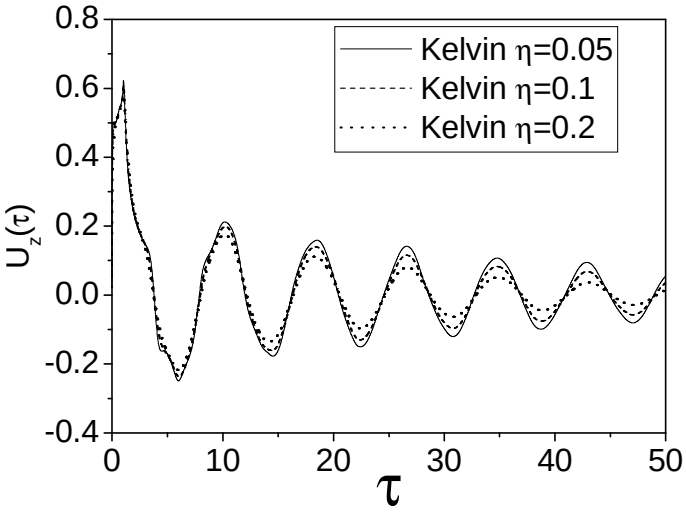

Figure 19: Displacement $u_z(t)$ for distinct values of the damping coefficient - Kelvin-Voigt model

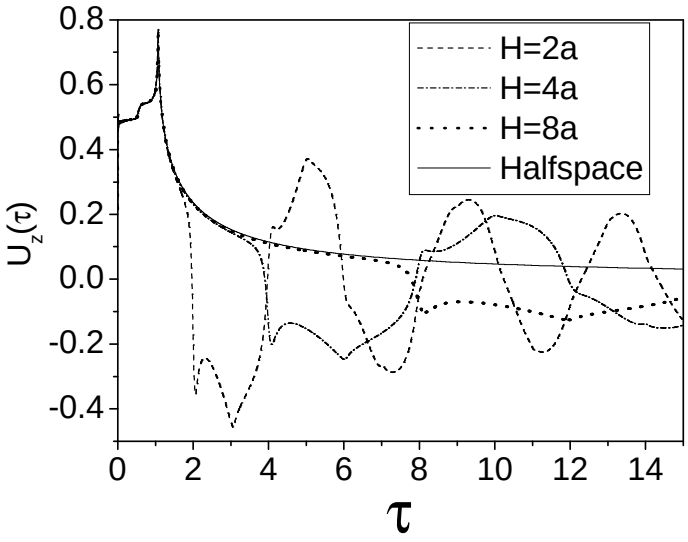

Figure 20: Effect of the layer depth on the transient response

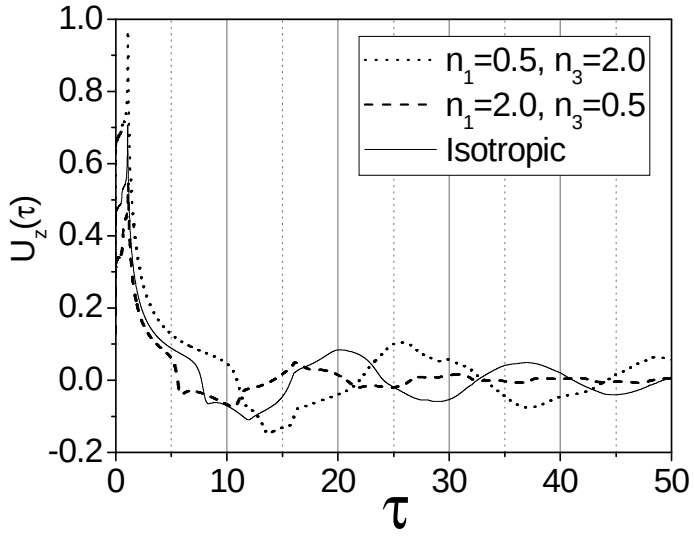

Figure 21: Response of a transversely isotropic layer: influence of the anisotropy degree

4.7 Influence of the layer degree of anisotropy.

The transient response of a transversely isotropic layer with depth $H = 8a$ is given in Figure 21. The constant hysteretic model with damping $\eta = 0.05$ is considered. The material properties for the isotropic layer are: $c_{11}/c_{44} = 4$. Two distinct cases are investigated. In the first case the anisotropy indices defined in equation are set to $n_1 = 2.0$, $n_3 = 0.5$. The basic effect of this setting is that the vertical stiffness, in the z-direction, is increased leading to a faster dilatational wave front and smaller travel times downward. The second choice of anisotropy indices is $n_1 = 0.5$, $n_3 = 2.0$. This causes a lower vertical stiffness, compared to the isotropic case and, consequently, smaller wave speeds with larger travel times. It should also be noted that for softer layers the response amplitude tends to increase significantly. All these features may be found in the response shown in Figure 21.

4.8 Analysis of causality.

It is well known that the FFT algorithm furnishes periodic responses. So, the response for the largest time $\tau_{\max}$ is connected to the initial time $\tau = 0$. This means that the response at $\tau_{\max}$ gives information about the causality of the obtained transient solution. Figures 22 and 23 give the influence of the damping model on the causal behavior of a typical layer. The last time steps of the response are depicted. It should be noted that a causal behavior would present a

vanishing solution at the last steps.

Figure 22 shows the effect of the damping ratio η for the constant hysteretic model. It is well known that this is a non-causal viscoelastic model [14]. In this model the static or quasi-static solution ($A_0 \to 0$) presents a non-vanishing complex part related to the material damping. In Figure 22, as the damping decreases and the solution tends to the causal elastic case, the transient response becomes increasingly causal. Figure 23 shows the effect of the damping model on the response causality for a damping ratio $\eta = 0.1$. It can be noticed that the Kelvin-Voigt model leads to a more causal response than the other analyzed models. Only at the very last time steps the K-V model shows some non-causal behavior. The results reported indicated that the present methodology may be used to assess the relation between damping models and causality.

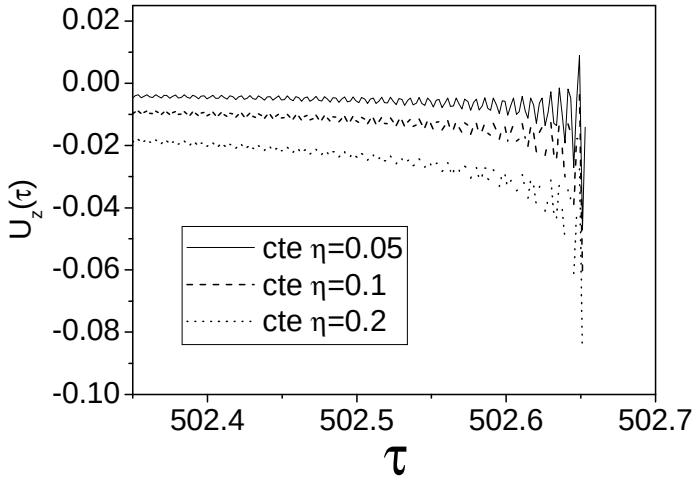

Figure 22: Analysis of causality - constant hysteretic model

5 Concluding Remarks

A methodology to synthesize numerical transient solutions for a viscoelastic and transversely isotropic layer resting on a rigid base under plain strain conditions has been presented. A series of original results were reported. Transient displacement and traction Green's functions and transient displacement fields for distributed loads solutions were determined. Short time and long term responses were obtained and explained in terms of the wave propagation and reflection phenomena. Snapshots of the displacement fields were furnished, creating the possibility to visualize the transient propagation phenomena. The obtained solutions allow to assess the

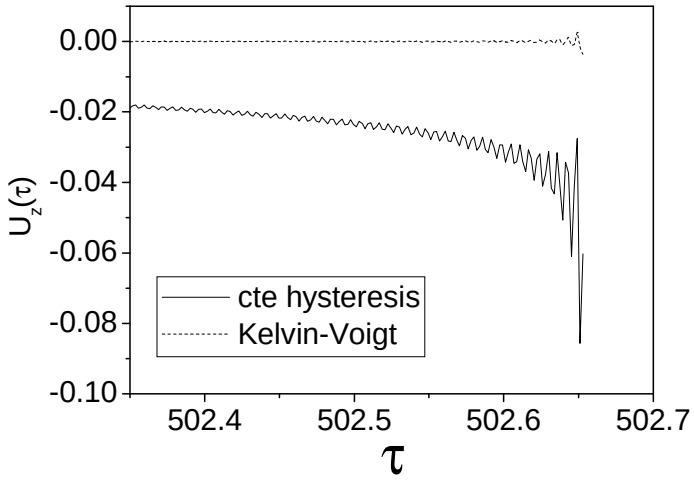

Figure 23: Analysis of causality - model comparison, $\eta = 0.1$

influence of viscoelastic models and parameters, as well as the degree of anisotropy of the continuum on the layer transient response. For the best of the authors' knowledge, in the literature, there are no comparable results reporting the response of unbounded viscoelastic and anisotropic domains. Furthermore, the transient displacement and traction solutions may be incorporated in a Boundary Element based methodology making possible the dynamic analysis of rigid and flexible surface foundations interacting with layered continua.

Acknowledgments: FAPESP, CAPES and FAEP have supported the research leading to the article. This is gratefully acknowledged.

References

[1] M. Adolph. Transient solutions for viscoelastodynamics problems in unbounded domains by the fast fourier transform. MS Thesis, Faculty of Mechanical Engineering, State University at Campinas (in Portuguese), 2002.

[2] P.L.A. Barros. Elastodynamics of transversely isotropic media: Green's functions and the boundary element method in the soil-structure interaction analysis. Ph. D. Thesis, Faculty of Mechanical Engineering, State University at Campinas (in Portuguese), 1997.

[3] P.L.A. Barros and E. Mesquita. Elastodynamic green's functions for orthotropic plane strain continua with inclined axis of symmetry. International Journal for Solids and Structures, 36:4767–4788, 1999.

[4] P.L.A. Barros and E. Mesquita. On the dynamic interaction and cross-interaction of 2d rigid structures with orthotropic elastic media possessing general principal axes orientation. Meccanica, 36(4):367–378, 2001.

[5] D.E. Beskos. Boundary element methods in dynamic analysis. Applied Mechanics Reviews, 40(1):01–23, 1987.

[6] D.E. Beskos. Boundary element methods in dynamic analysis: Part II (1986-1996). Applied Mechanics Reviews, 50(3):149–197, 1997.

[7] R.M. Christensen. Theory of viscoelasticity. Academic Press, NY, 1982.

[8] J. Dominguez. Boundary Elements in Dynamics. Computational Mechanics Publications, Southampton, UK, 1993.

[9] L. Gaul and M. Schanz. A comparative study of three boundary element approaches to calculate the transient response of viscoelastic solids with unbounded domains. Computational Mechanics, 179:111–123, 1999.

[10] L. Gaul, M. Schanz, and C. Fiedler. Viscoelastic formulations of bem in time and frequency domain. Eng. Analysis with Boundary Elements, 10:137–141, 1992.

[11] G. Gazetas. Analysis of machine foundation vibrations: state of the art. Soil Dynamics and Earthquake Engineering, 2(1):2–42, 1983.

[12] F. Guan and M. Novak. Transient response of an elastic homogeneous halfspace to suddenly applied rectangular loading. Geotechnical Research Centre Report GEOT-10-92, 1992.

[13] W.S. Hall and G. Oliveto. Boundary Element Methods for Soil-Structure Interaction. Kluwer Academic Publishers, 2003.

[14] N. Makris and J. Zhang. Time-domain viscoelastic analysis of earth structures. Earthquake Engineering and Structural Dynamics, 29:745–768, 2000.

[15] G.D. Manolis and D.E. Beskos. Boundary Element Methods in Elastodynamics. Unwin Hyman Ltd., London, UK, 1988.

[16] A.D. Mesquita and H.B. Coda. An alternative time integration procedure for boltzmann viscoelaticity: A bem apporach. Computer and Structures, 79(16):1487–1496, 2001.

[17] A.D. Mesquita and H.B. Coda. Boundary integral equation method for the general viscoelastic analysis. International Journal of Solids and Structures, 39(9):2643–2664, 2002.

[18] E. Mesquita, M. Adolph, P.L.A. Barros, and E. Romanini. Transient green and influence functions for plane strain visco-elastic half-spaces. Proceedings of the IABEM SYMPOSIUM, The University of Texas at Austin, May 28-31, pages 1–12, 2002.

[19] C. Richter. A Green's Function time-domain BEM of Elastodynamics. Computational Mechanics Publications, Southamptom UK, 1997.

[20] M. Schanz and H. Antes. A new visco- and elastodynamic time domain boundary element formulation. Computational Mechanics, 20(5):452–459, 1997.

[21] A. Sommerfeld. Partial Differential Equations. Academic Press, New York, 1949.